Electrochimica Acta 211 (2016) 420–429

Contents lists available at ScienceDirect

Electrochimica Acta

journal homepage: www.elsevier.com/locate/electacta

Simulations and Interpretation of Three-Electrode Cyclic Voltammograms of Pseudocapacitive Electrodes

Henri-Louis Girard[a], Bruce Dunn[b], Laurent Pilon[a,*]

[a] University of California Los Angeles, Henry Samueli School of Engineering and Applied Science, Mechanical and Aerospace Engineering Department, 420 Westwood Plaza, Los Angeles, CA 90095, USA
[b] University of California Los Angeles, Henry Samueli School of Engineering and Applied Science, Material Science and Engineering Department, 410 Westwood Plaza, Los Angeles, CA 90095, USA

ARTICLE INFO

Article history:
Received 7 April 2016
Received in revised form 11 June 2016
Accepted 13 June 2016
Available online 23 June 2016

ABSTRACT

This study aims to provide physical interpretation of cyclic voltammograms obtained from pseudocapacitive electrodes using three-electrode systems. It presents numerical simulations based on a recent continuum model able to reproduce experimental CV curves obtained with different Nb_2O_5-based electrodes and $LiClO_4$ in propylene carbonate as electrolyte. First, the respective contributions of faradaic and electric double layer charge storage mechanisms were clearly identified along with the associated faradaic and capacitive regimes. This was further illustrated by comparing CV curves for pseudocapacitive (Nb_2O_5) and EDLC (carbon) electrodes. Transition from the faradaic to the capacitive regime was caused by Li^+ starvation at the electrode/electrolyte interface and the formation of ClO_4^- electric double layer. Moreover, the effects of electrode crystallinity on CV curves were reproduced and interpreted in terms of enhanced transport properties for lithium intercalation and electrode electrical conductivity. Finally, the electrode thickness featured an optimum corresponding to a compromise between accommodating large amounts of intercalated lithium and minimizing the potential drop across the electrode to drive faradaic reactions.

1. Introduction

The most common electrochemical capacitors (ECs), generally known as supercapacitors or electric double layer capacitors (EDLCs), store charge physically by the adsorption of ions in a thin double layer at the interface between the electrode, typically carbon, and the liquid electrolyte [1]. It is well established that these carbon-based supercapacitors possess a number of attractive properties including fast charging, the delivery of significantly more power than batteries, and long cycle life. Pseudocapacitance represents a second capacitive energy storage mechanism. Pseudocapacitors store charge both physically in the electric double layer (EDL) and chemically by changing the oxidation state of the electrode material [2–5].

The energy density associated with redox reactions can be 10 times greater than that of double layer processes. Thus, pseudocapacitor materials offer the prospect of achieving the energy densities of batteries combined with thepower density of EDLCs. For that reason, there has been substantial interest in the synthesis and characterization of materials that exhibit pseudocapacitive charge storage [2–5].

Pseudocapacitive materials have often relatively poor solid-state diffusion and electrical conductivity which limits the practical thickness of the electrode and its energy and power densities. In order to mitigate the slow intercalation and/or the potential drop across the electrode several approaches can be envisioned. First, the thickness can be adjusted to reduce the electrode electrical resistance and the intercalation distance. The materials can also be synthesized with different crystalline structures to achieve larger electrical conductivity and faster intercalation [6]. Our recent work with Nb_2O_5 (orthorhombic form) established that upon lithium insertion, this material was able to exhibit high levels of energy storage, nearly 120 mAh g^{-1} at a charging rate of 1 minute (nominally 60C) [5]. We characterized the electrochemical properties of the Nb_2O_5 and determined that the kinetics of charge storage was unusually fast thanks a crystalline network offering easy transport pathways. Another key feature with this material is that there is no phase transformation upon lithiation [7]. Indeed, phase transitions lead to slower and less reversible ion diffusion in the electrode material indicated by the presence of additional peaks in the cyclic voltammetry curves [7].

---

* Corresponding author. Tel.: +1 (310) 206 5598; fax: +1 (310) 206 2302.
E-mail address: pilon@seas.ucla.edu (L. Pilon).

http://dx.doi.org/10.1016/j.electacta.2016.06.066
0013-4686/

Nomenclature

a_i	Effective ion diameter of species i (nm)
b	b-value, power constant in $j_t = a\nu^b$
c_i	Ion concentration in the electrolyte of species i (mol/L)
$c_{i,max}$	Maximum ion concentration, $c_{i,max} = 1/N_A a^3$ (mol/L)
$C_{s,int}$	Integral areal capacitance (F/m^2)
$c_{1,P}$	Concentration of intercalated Li in the pseudocapacitive electrode (mol/L)
$c_{1,P,0}$	Initial concentration of intercalated Li
$c_{1,P,max}$	Maximum concentration of intercalated Li, $c_{1,C,max} = m\,\rho/M$ (mol/L)
D_i	Diffusion coefficient of ions in electrolyte (m^2/s)
$D_{1,P}$	Diffusion coefficient of intercalated Li in the pseudocapacitive electrode (m^2/s)
e	Elementary charge, $e = 1.602 \times 10^{-19}$ C
F	Faraday constant, $F = eN_A = 9.648 \times 10^4$ C mol^{-1}
H	Stern layer thickness (nm)
j_C	Magnitude of predicted capacitive current density (A/m^2)
j_F	Magnitude of predicted faradaic current density (A/m^2)
j_T	Magnitude of predicted total current density (A/m^2)
k_0	Reaction rate constant, Equation (14)(m$^{2.5}$mol$^{-0.5}$s^{-1})
L	Electrolyte thickness (nm)
L_P	Thickness of the pseudocapacitive electrode (nm)
m	Stoichiometric number of intercalated Li, $Li_mM_pO_q$
M	Molecular weight of the fully intercalated active electrode material (g/mol)
n_c	Cycle number
N_A	Avogadro constant, $N_A = 6.022 \times 10^{23}$ mol^{-1}
N_i	Ion flux of species i (mol m^{-2}s^{-1})
p, q	Stoichiometric numbers of the metal and oxygen in the metal oxide M_pO_q
R_u	Universal gas constant, $R_u = 8.314$ J mol^{-1}K^{-1}
T	Local temperature (K)
t	Time (s)
ν	Scan rate of the cyclic voltammetry (V/s)
x	Location in one-dimensional space (μm)
z_i	Ion valency of species i

Greek symbols

α	Transfer coefficient, Equations (13) and (14)
ϵ_0	Vacuum permittivity, $\epsilon_0 = 8.854 \times 10^{-12}$ F m^{-1}
ϵ_r	Relative permittivity of electrolyte
$\Delta\psi_{eq}$	Equilibrium potential difference (V)
$\Delta\psi_H$	Potential drop across the Stern layer (V)
λ_D	Debye length (m)
η	Overpotential, $\eta = \Delta\psi_H - \Delta\psi_{eq}$ (V)
ρ	Density of the fully intercalated pseudocapacitive electrode material (kg/m^3)
σ_P	Electrical conductivity of the electrode (S/m)
τ_{CV}	Cycle period (s)
ψ	Electric potential (V)
ψ_{min}, ψ_{max}	Minimum and maximum of the potential window (V)
ψ_s	Imposed cell potential (V)

Superscripts and subscripts

∞	Refers to bulk electrolyte
i	Refers to ion species i ($i = 1$ for $Li^{\pm}$ and $i = 2$ for ClO_4^-)
P	Refers to the pseudocapacitive electrode

Electrochemical studies of pseudocapacitor materials are generally of the three-electrode type. In this configuration, the pseudocapacitor material serves as the working electrode, with a porous carbon electrode as the counter electrode and a reference electrode that controls the potential at the working electrode. For the research on Nb_2O_5, where we were investigating the insertion and de-insertion of lithium ions, Li metal served as both the counter and the reference electrode [5]. The benefit of three-electrode studies is that one is able to characterize a single material, in contrast to experiments with a traditional two-electrode device where the properties of a given electrode material are inferred. Our previous simulation studies that were used to characterize electric double layer capacitors with asymmetric electrolytes or hybrid pseudocapacitors were based on two-electrode configurations [8–12]. While these studies are extremely useful for providing insight on device characteristics, they are not designed to contribute detailed understanding of the electrode material, which is frequently the focus of experimental studies on pseudocapacitors. Indeed, the current in two-electrode hybrid pseudocapacitors is controlled by the carbon electrode whereas the current in three-electrode measurements is only limited by redox reactions and interfacial and transport phenomena through or near the pseudocapacitive electrode. Consequently, the equilibrium potential and the state of charge may vary significantly and must be accounted for.

The objective of the present study is to connect numerical simulations directly to experimental studies by simulating three-electrode configurations with a Nb_2O_5 working electrode. Our approach involves the use of numerical simulations based on a continuum model previously described [10,11]. The results provide physical interpretation of the experimentally measured cyclic voltammograms obtained from three-electrode measurements on Nb_2O_5 electrodes and characterize the interplay between faradaic and EDL charge storage mechanisms. Furthermore, this study illustrates how the physical model and the associated simulation tools can be used to optimize the design of individual pseudocapacitive electrodes.

2. Analysis

2.1. Schematic and Assumptions

Fig. 1 shows a schematic of the simulated domain and of the associated coordinate system. The domain consisted of a pseudocapacitive electrode of thickness L_P made of metal oxide M_pO_q and a binary and symmetric electrolyte of thickness L containing lithium salt in a solvent at high concentration. The electrolyte was further divided in two regions (i) a Stern layer of thickness H defining the distance of closest approach of the ions to the electrode and (ii) a diffuse layer where the ions were free to move under the combined influence of electrodiffusion and steric repulsion [13]. The origin $x = 0$ was located in the bulk of the electrolyte far from the electrode, i.e., $L \gg \lambda_D$ where λ_D is the Debye length characterizing the thickness of the double layer. For a binary symmetric electrolyte it is defined as $\lambda_D = \left(\epsilon_0\epsilon_r R_u T/2F^2 z_1^2 c_{1,\infty}\right)^{1/2}$. The model used in this study was based on the generalized modified Poisson-Nernst-Planck (GMPNP) model for binary symmetric electrolyte with faradaic reactions. This model and the underlying assumptions were described in detail in Ref. [10] and need not be repeated. In brief, the main assumptions include (1) the Stern layer thickness H was taken as the radius of solvated ClO_4^- ions (2) the dielectric constant of the electrolyte was taken as constant and equal to 64.4 corresponding to PC [14], (3) the reversible redox reaction occurred at the electrode/electrolyte interface transferring Li^+ from the electrolyte into the M_pO_q matrix, (4) Li^+ intercalation, accompanied by reduction of the transition metal cations in the

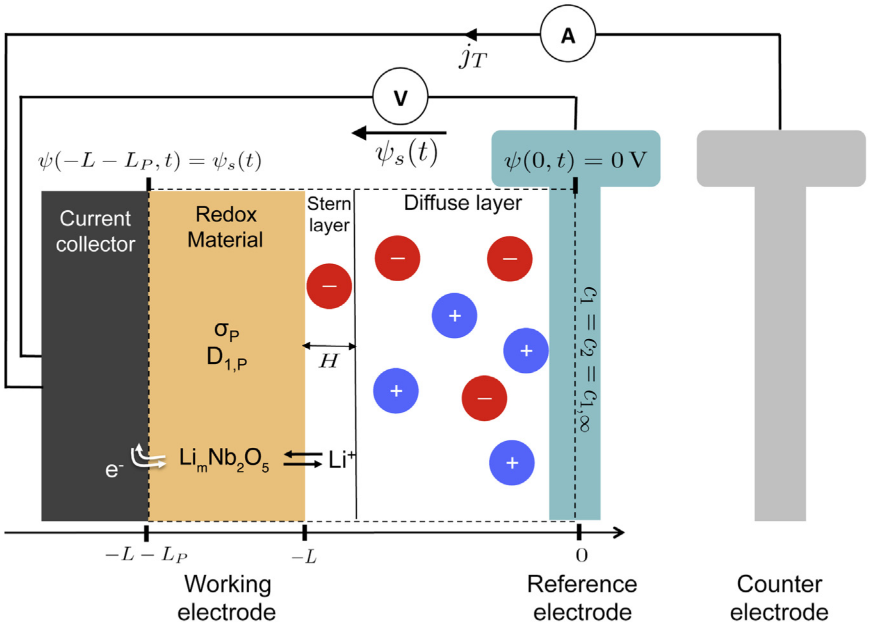

Fig. 1. Schematic of the simulated one-dimensional pseudocapacitive electrode consisting of a redox-active pseudocapacitive electrode in a three-electrode setup with $LiClO_4$ in propylene carbonate as electrolyte. The dashed line encloses the computational domain simulated.

electrode, was treated as one-dimensional diffusion processes, (5) The physicochemical properties of the electrodes and the electrolyte were assumed to be constant, and (6) the electrode material did not undergo any phase transition during the lithiation process, as observed experimentally [5,7]. The governing equations are reproduced in Appendix A for convenience. They consisted of the conservation equations governing the spatiotemporal evolution of (i) the potential $\psi(x, t)$ in the electrode and electrolyte, (ii) the ion concentrations $c_1(x, t)$ and $c_2(x, t)$ for Li^+ and ClO_4^- ions in the electrolyte, respectively, and (iii) the intercalated Li concentration $c_{1,P}(x, t)$ in the electrode.

The three-electrode measurement method consists of (1) the working electrode under investigation, (2) a reference electrode setting the reference potential, and (3) a counter-electrode designed to measure the current without limiting it. This method ensures that no current flows through the reference electrode and its potential remains constant. It also enables precise control of the potential between the electrolyte and the pseudocapacitive working electrode. In our simulations, a triangular potential waveform $\psi_s(t)$ was imposed at the current collector $(x=-L-L_P)$ [10]. On the other hand, the potential in the bulk of the electrolyte was set as $\psi(x=0, t)=0\,\mathrm{V}$. This set the reference potential for the system in a way similar to the reference electrode in the experimental setup. Additionally, the ion concentrations $c_1(x, t)$ and $c_2(x, t)$ were imposed to be constant at $x=0$ and equal to their bulk concentrations, i.e., $c_1(0, t)=c_2(0, t)=c_{1,\infty}$. This prevented the formation of an EDL and ensured that the reference electrode did not pass any current. No condition was imposed on the current flowing at the electrode/current collector interface to account for the overcapacitive counter-electrode used experimentally.

2.2. Constitutive Relationships

A total of 15 input parameters were needed to solve the governing equations, initial and boundary conditions including (i) the binary and symmetric electrolyte properties, comprising the permittivity ϵ_r, the Li^+ ion diameter a_1, valency z_1, diffusion coefficient D_1, and bulk concentration $c_{1,\infty}$, (ii) the pseudocapacitive electrode properties namely the electrical conductivity σ_P, the Li diffusion coefficient $D_{1,P}$, the initial Li concentration $c_{1,P,0}$, the reaction rate constant k_0, and the equilibrium potential for the redox reaction $\Delta\psi_{eq}$, (iii) the cell dimensions including the electrolyte thickness L and the electrode thickness L_P, and (iv) the operating conditions, i.e., the temperature T, the potential window defined by ψ_{max} and ψ_{min}, and the scan rate v.

Table 1 summarizes the values of these input parameters for the baseline case corresponding to Nb_2O_5 electrode with an electrolyte containing Li^+ ions in propylene carbonate (PC). The properties were taken from the literature whenever possible. The counter-ion

Table 1
Electrode and electrolyte properties and dimensions used in the simulations reported in this study

Parameters	Symbol	Value	Unit	Ref.
Relative permittivity	ϵ_r	64.4		[14]
Ion diameter	$a_1=a_2$	0.67	nm	[15]
Ion valency	$z_1=-z_2$	1		
Ion diffusion coefficient	$D_1=D_2$	2.6×10^{-10}	m^2/s	[15]
Stern layer thickness	H	0.5	nm	[9]
Initial bulk ion concentration	$c_{1,\infty}=c_{2,\infty}$	1	mol/L	[16–18]
Electrode conductivity	σ_P	10^{-4} to 10^{-3}	S/m	[19]
Intercalated Li diffusion coefficient	$D_{1,P}$	10^{-14} to 10^{-11}	m^2/s	[20]
Reaction rate	k_0	10^{-8}	$m^{2.5}mol^{-0.5}s^{-1}$	[20–22]
Transfer coefficient	α	1/2		
Maximum intercalated Li concentration	$c_{1,P,max}$	32.9	mol/L	[23]
Initial intercalated Li concentration	$c_{1,P,0}$	1 to 5	mol/L	[23]
Electrolyte thickness	L	1	μm	
Electrode thickness	L_P	20 to 150	nm	[27,24]
Temperature	T	298	K	
Potential window	$\psi_{max}-\psi_{min}$	0.9	V	[16–18]
Scan rate	v	0.5 to 10	V/s	[16–18]

in the binary symmetric electrolyte had opposite valency $z_2 = -z_1$ but diameter a_2, diffusion coefficient D_2, and bulk concentration $c_{2,\infty}$ identical to those of Li$^+$. Note that the permittivity ϵ_r of the electrolyte was considered constant and independent of the electric field. Furthermore, the equilibrium potential difference $\Delta\psi_{eq}$, also known as the open circuit potential, varies with the oxidation state of the electrode [25]. This variation is commonly assumed to be linear [25]. The fitting parameters were measured for a MnO_2 electrode in KOH electrolyte with potassium intercalation as a function of the state of charge $c_{1,P}/c_{1,P,max}$ where $c_{1,P,max}$ corresponds to the maximum intercalated Li concentration [25]. In the absence of experimental data for Nb_2O_5, parameters for MnO_2 were used to account for the evolution of the equilibrium potential difference with the state-of-charge [25]

$$\Delta\psi_{eq}(t) = 10.5\left(4 - \frac{c_{1,P}(t)}{c_{1,P,\max}}\right) - 39.9. \qquad (1)$$

The maximum concentration $c_{1,P,max}$ corresponding to fully-lithiated $Li_2Nb_2O_5$ was taken as 32.9 mol/L. In order to preserve the continuity of all variables from the imposed initial conditions, the initial equilibrium potential was required to be zero, i.e., $\Delta\psi_{eq}(t=0) = 0$ V. This condition was satisfied by setting the initial Li concentration in the electrode as $c_{1,P}(0) = c_{1,P,0} = 6.578$ mol/L. In the baseline case, the pseudocapacitive electrode had thickness $L_P = 50$ nm, electrical conductivity $\sigma_P = 10^{-4}$ S/m, and Li diffusion coefficient $D_{1,P} = 10^{-12}$ m^2/s, corresponding to realistic values [19,20]. Finally, the numerically predicted CV curves corresponding to oscillatory steady-state were compared with experimental measurements for electrodes made of Nb_2O_5 with $LiClO_4$ in PC as electrolyte [5,6,26].

3. Results and Discussion

3.1. Voltammogram interpretation

Fig. 2a shows CV curves obtained from three-electrode experimental CV measurements at different scan rates. The electrode consisted of T-Nb_2O_5 (orthorhombic) nanocrystal mixed 1:1 with carbon black on a stainless steel current collector with 1 mol/L $LiClO_4$ in PC as electrolyte [5]. Similarly, Fig. 2b plots the numerical predictions corresponding to the baseline case (Table 1). Fig. 2 indicates that the overall shapes of the experimentally measured and numerically predicted CV curves were similar. The CV curves featured a large current density in the lower portion of the potential window and a significantly smaller current at higher potentials. The evolution of the CV curves with increasing scan rate also followed a similar trend with the charging and discharging peak increasing in magnitude and shifting to lower and higher potentials, respectively. Finally, the shape of the CV curves during the potential reversal between charging and discharging became more round with increasing scan rate. This can be attributed to the increasingly resistive behavior. Indeed, the potential at the electrode/electrolyte interface ($x = -L$) became significantly lower and varied more slowly than the potential $\psi_s(t)$ imposed at the current collector ($x = -L - L_P$) as the scan rate increased. This delayed the EDL formation and reduced the electrode surface overpotential driving the redox reaction.

To further elucidate these observations, Fig. 3a shows the numerically predicted (i) capacitive current density $j_C(t)$ due to EDL formation and dissolution, (ii) the faradaic current density $j_F(t)$ associated with reversible redox reactions, and (iii) the total current density $j_T(t) = j_C(t) + j_F(t)$ as functions of the imposed potential $\psi_s(t)$ for the baseline case at scan rate $v = 5$ V/s. Fig. 3b shows the corresponding concentrations $c_1(-L+H, t)$ of the cation Li$^+$ and $c_2(-L+H, t)$ of the anion ClO_4^- at the Stern/diffuse layer interface while Fig. 3c shows the intercalated lithium concentration $c_{1,P}$ at the electrode/electrolyte interface. The CV curve displays two regimes: (i) the faradaic regime in the lower portion of the potential window when the total current density was dominated by the faradaic current, i.e., $j_T(t) \approx j_F(t)$, and (ii) the capacitive regime in the upper end of the potential window when the capacitive current dominated, i.e., $j_T(t) \approx j_C(t)$, and the overall current magnitude was smaller than in the faradaic regime. Fig. 3b indicates that the anions ClO_4^- formed the EDL during the capacitive regime. Their concentration $c_2(-L+H, t)$ at the Stern/diffuse layer interface near the pseudocapacitive electrode reached the maximum packing concentration of 5.52 mol/L quickly after the onset of the capacitive regime, marked by a red circle. Symmetrically, the cations Li$^+$ were repelled and their concentration $c_1(-L+H, t)$ at the electrode surface was negligible during the capacitive regime. The steep drop in

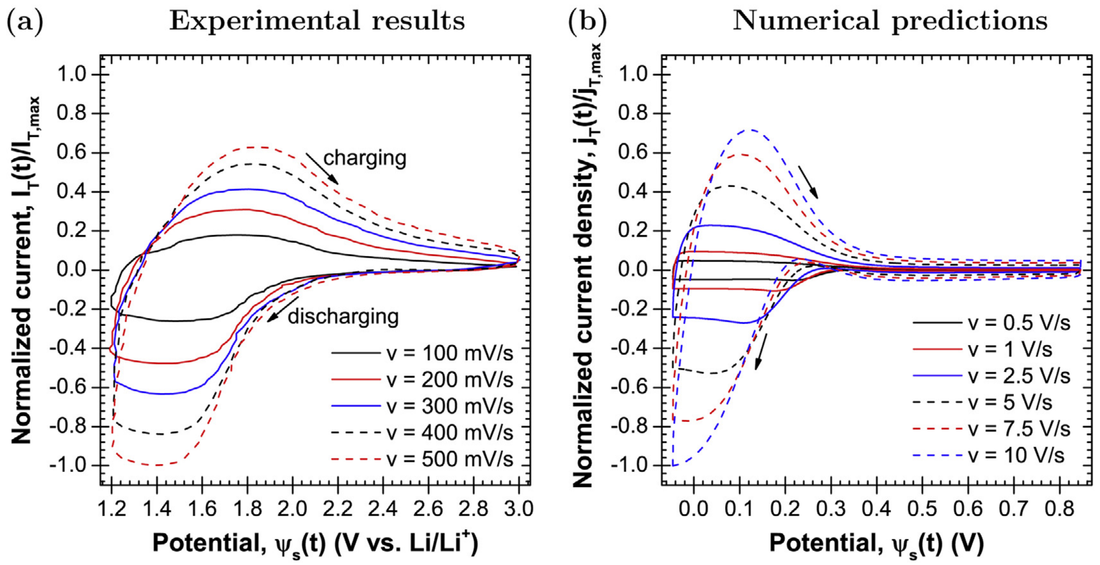

Fig. 2. (a) Experimental measurements of the total current $I_T(t)$ scaled by the absolute value of the maximum current as a function of imposed potential $\psi_s(t)$ for a pseudocapacitive electrode consisting of T-Nb_2O_5 (orthorhombic) nanocrystal mixed 1:1 with carbon black on a stainless steel current collector with 1 mol/L $LiClO_4$ in PC as electrolyte reported in Figure 1a of Ref. [5]. (b) Numerically predicted total current density $j_T(t)$ scaled by the absolute value of the maximum current density as a function of imposed potential $\psi_s(t)$ for different scan rates v ranging from 0.5 to 10 V/s.

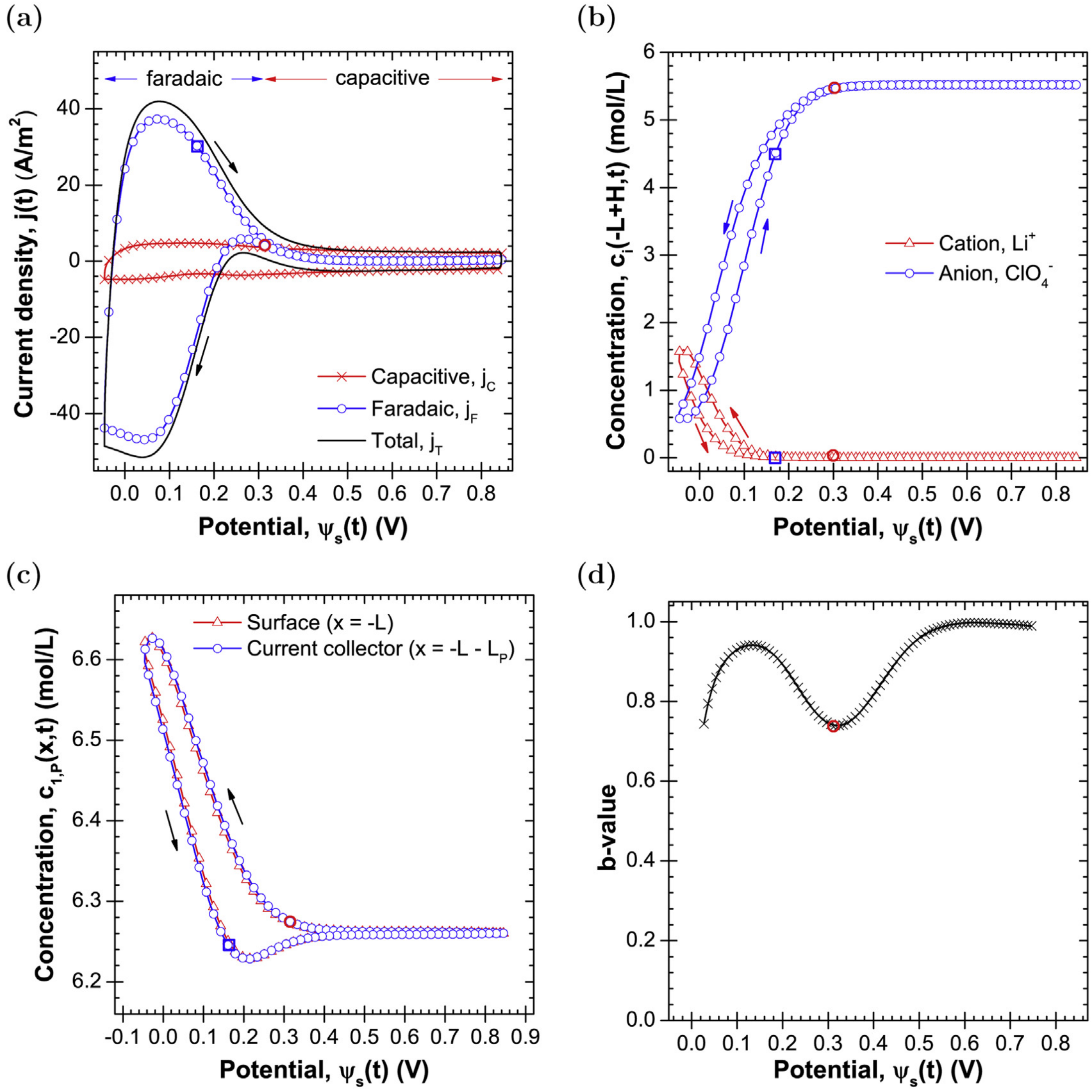

Fig. 3. (a) Numerically predicted capacitive j_C, faradaic j_F, and total j_T current densities as functions of imposed potential $\psi_s(t)$ for the baseline pseudocapacitive electrode at scan rate $v = 5$ V/s. (b) Concentrations of the cation Li$^+$ $c_1(-L+H, t)$ and of the anion ClO_4^- $c_2(-L+H, t)$ at the Stern/diffuse layer interface near the pseudocapacitive electrode ($x = -L+H$) as functions of imposed potential $\psi_s(t)$. (c) Predicted b-value as a function of imposed potential $\psi_s(t)$ for constitutive relationships corresponding to the baseline case.

the faradaic current observed in the CV curves during discharging was due to the starvation of Li$^+$ ions at the electrode/electrolyte interface necessary for the faradaic reaction. The onset of Li$^+$ ion starvation is indicated by a blue square in Fig. 3a to 3c. Note also that the simulated scan rates were larger than those used in experimental measurements. This was due to the fact that diffusion limitation and Li$^+$ ion starvation appeared at a much higher scan rate for the simulated planar electrode than for the actual porous electrodes.

Fig. 3d shows the b-value, obtained from fitting the evolution of current density with scan rate according to the power law $j_T(\psi_s) = a(\psi_s)v^{b(\psi_s)}$ as a function of imposed potential $\psi_s(t)$, as commonly performed experimentally [16,27–29]. Fig. 3d indicates that a dip in b-value occurred for potentials $\psi_s(t)$ around 0.3 V. Such a dip was also observed in three-electrode experimental measurements and attributed to the oxidation of the metal oxide [29]. However, the numerical simulations established that the dip in the b-value coincided with the transition between the faradaic and the capacitive regimes (red circle) [10,11]. This transition corresponded to the steep drop in the total current density observed in both experimental data and numerical simulations shown in Fig. 2.

3.2. Comparison with equivalent EDL electrode

Fig. 4a compares experimental CV curves at 2 mV/s in terms of specific current i_T (in A/g) for an electrode made of carbon nanotubes and for a pseudocapacitive electrode consisting of T-Nb_2O_5 (orthorombic) with 1 mol/L $LiClO_4$ in PC as electrolyte and Li metal for the counter and reference electrodes [26]. Similarly, Fig. 4b shows the numerically predicted CV curves at 1 V/s for the baseline pseudocapacitive electrode previously defined as well as for an equivalent electrode in which charge storage was exclusively through EDL formation. The density of carbon and Nb_2O_5 were taken as 2250 and 4550 kg m^{-3}, respectively. Here also, numerical and experimental results show similar behavior for both types of electrodes. The EDLC or carbon electrode displayed a rectangular CV curve characteristic of capacitive behavior. On the other hand, the pseudocapacitive electrode featured a large current in the lower portion of the potential window. Interestingly, in both experimentally measured and numerically simulated CV curves, the current density of the pseudocapacitive electrode, in the upper end of the potential window, corresponding to the capacitive regime, matched that of the carbon electrode. This confirms that,

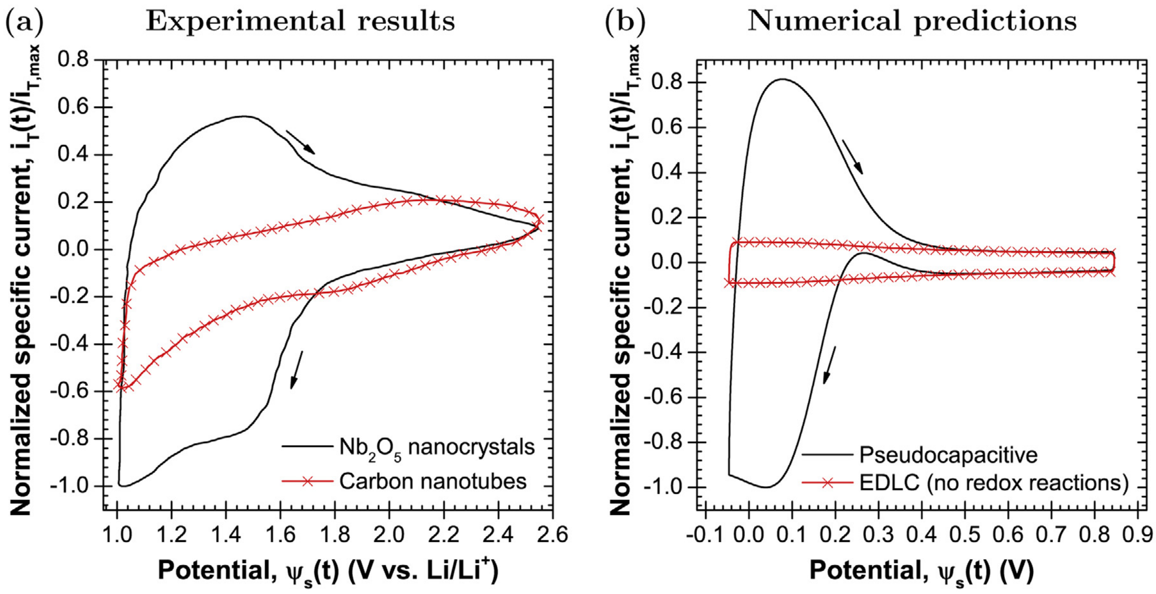

Fig. 4. (a) Experimental CV curves in terms of the total current $I_T(t)$ scaled by the absolute value of the maximum current as a function of imposed potential $\psi_s(t)$ at 2 mV/s. Here, the pseudocapacitive electrode consisting of 5 nm Nb_2O_5 nanocrystal mixed with PVDF (10%) and carbon black (10%) with 1 mol/L $LiClO_4$ in PC as electrolyte and Li metal for the counter and reference electrodes as well as an equivalent electrode consisting of carbon nanotubes (EDLC). The experimental data was retrieved from Figure 3a of Ref. [26]. (b) Numerically predicted CV curves in terms of the total current $I_T(t)$ scaled by the absolute value of the maximum current as a function of imposed potential $\psi_s(t)$ at 1 V/s for the pseudocapacitive electrode considered in the baseline case as well as for an equivalent EDL electrode.

in this potential region, EDL formation was the main mechanism for charge storage. Such comparison provides an experimental way to distinguish the capacitive from the faradaic regime and to estimate the contribution of EDL formation to charge storage for a given electrolyte. As previously explained, the simulated scan rate was significantly larger than that imposed experimentally. This resulted in significantly larger current densities. In other words, simulating planar electrodes replicates experimental measurements only qualitatively but can provide significant insights lacking from experimental measurements. Quantitative predictions with realistic scan rates and current densities should be achievable by simulating actual three-dimensional electrode architectures, albeit at significant computational cost.

3.3. Crystalline vs. amorphous pseudocapacitive material

Niobium oxide can assume different phases depending on the synthesis method. The most common structures are amorphous, pseudo-hexagonal (TT-Nb_2O_5), and orthorhombic (T-Nb_2O_5). These phases exhibit different electrical conductivity σ_P and Li diffusion coefficient $D_{1,P}$. In particular, crystalline phases display larger electrical conductivity than the amorphous phase due to the increased domain size enabling the charge carriers to follow crystalline pathways [6]. They also feature larger solid-state diffusion coefficient due to the creation of diffusion pathways in the crystalline structure with low energy barrier for easier intercalation [30].

Fig. 5a shows experimental CV curves at 10 mV/s for pseudocapacitive electrodes consisting of (i) T-Nb_2O_5 (orthorombic) nanoparticles or (ii) amorphous Nb_2O_5 nanoparticles on a stainless steel current collector with 1 mol/L $LiClO_4$ in PC as electrolyte and Li metal for the counter and reference electrodes [6]. Similarly, Fig. 5b shows numerically predicted CV curves for $v = 5$ V/s for a pseudocapacitive electrode with (i) high conductivity ($\sigma_P = 10^{-3}$ S/m) and fast Li diffusion ($D_{1,P} = 10^{-12}$ m^2/s) simulating crystalline Nb_2O_5 and (ii) an electrode with lower conductivity ($\sigma_P = 10^{-4}$ S/m) and slower diffusion ($D_{1,P} = 10^{-14}$ m^2/s) corresponding to amorphous Nb_2O_5. All other properties were the same as in the baseline case (Table 1). Here also, numerical and experimental CV curves display very similar shapes and trends for both amorphous and crystalline electrode materials. They indicate that the capacitance was significantly larger for the crystalline phase of Nb_2O_5 thanks to better transport properties leading to faster intercalation and smaller electrical resistance. However, the current density in the capacitive regime ($\psi_s > 0.3$ V) appeared to be independent of the phases. This can be attributed to the fact that charge storage was achieved only by EDL formation at the electrode/electrolyte interface and to the absence of faradaic reactions and Li$^+$ intercalation.

3.4. Effect of Electrode Thickness

Fig. 6a shows the numerically predicted CV curves in terms of total current density j_T as a function of imposed potential $\psi_s(t)$ for different values of pseudocapacitive electrode thickness L_P ranging from 5 to 150 nm at scan rate $v = 1$ V/s. All parameters other than L_P corresponded to the baseline case (Table 1). Fig. 6a indicates that, as the electrode thickness increased, the magnitude of the peak current initially increased. However, the shape of the CV curve became more rounded and the peak current decreased beyond a certain thickness. This was due to the increasingly resistive behavior caused by the potential drop across the thicker electrode, as previously discussed.

Fig. 6b shows the electrode integral capacitance $C_{s,int}$ at low scan rate (i.e., under quasi-equilibrium) as a function of the thickness of the pseudocapacitive electrode L_P. For the parameters of the baseline case considered in this study, the optimal electrode thickness was around $L_P = 65$ nm. These results illustrate the trade-off faced when designing a pseudocapacitive electrode between offering a large electrode volume for redox intercalation while maintaining acceptable potential drop across the electrode to drive the faradaic reactions. Among all parameters, increasing the electrode thickness and/or the diffusion coefficient of Li$^+$ in the pseudocapacitive electrode had the most beneficial effects on the electrode performance. Larger electrical conductivity was also beneficial when the

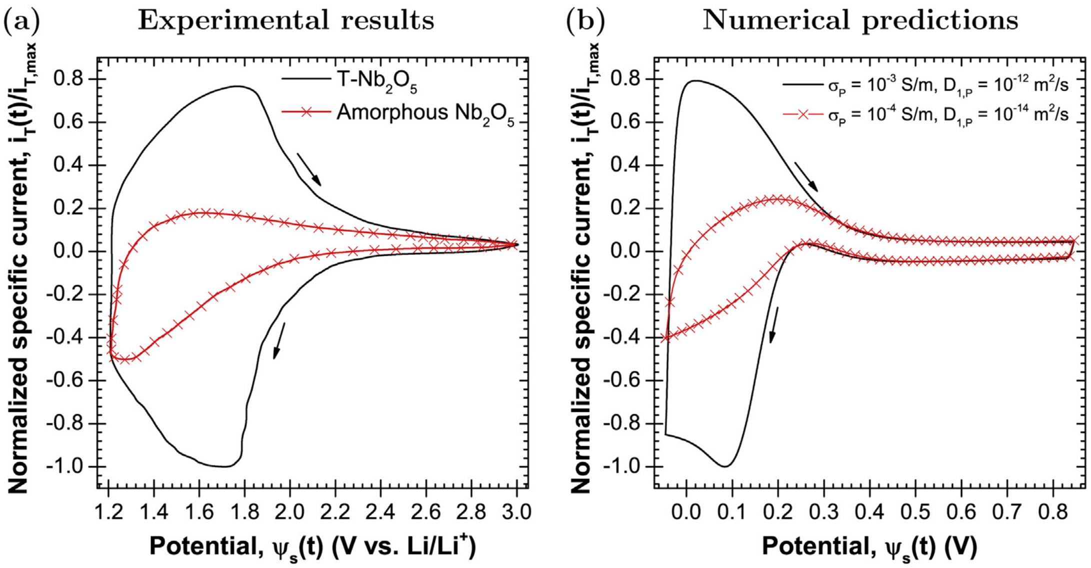

Fig. 5. (a) Experimental CV curves in terms of the total current $I_T(t)$ scaled by the absolute value of the maximum current as a function of imposed potential $\psi_s(t)$ for a pseudocapacitive electrode consisting of T-Nb_2O_5 (orthorombic) nanoparticles on a stainless steel current collector with 1 mol/L $LiClO_4$ in PC as electrolyte and Li metal for the counter and reference electrodes as well as a pseudocapacitive electrode consisting of amorphous Nb_2O_5 in the same conditions. The experimental data was retrieved from Figure 4a of Ref. [6]. (b) Numerically predicted CV curves in terms of the total current $I_T(t)$ scaled by the absolute value of the maximum current as a function of imposed potential $\psi_s(t)$ for a pseudocapacitive electrode with high conductivity ($\sigma_P = 10^{-3}$ S/m) and fast Li diffusion ($D_{1,P} = 10^{-12}$ m^2/s) as well as for a pseudocapacitive electrode with low conductivity ($\sigma_P = 10^{-4}$ S/m) and slow diffusion ($D_{1,P} = 10^{-14}$ m^2/s).

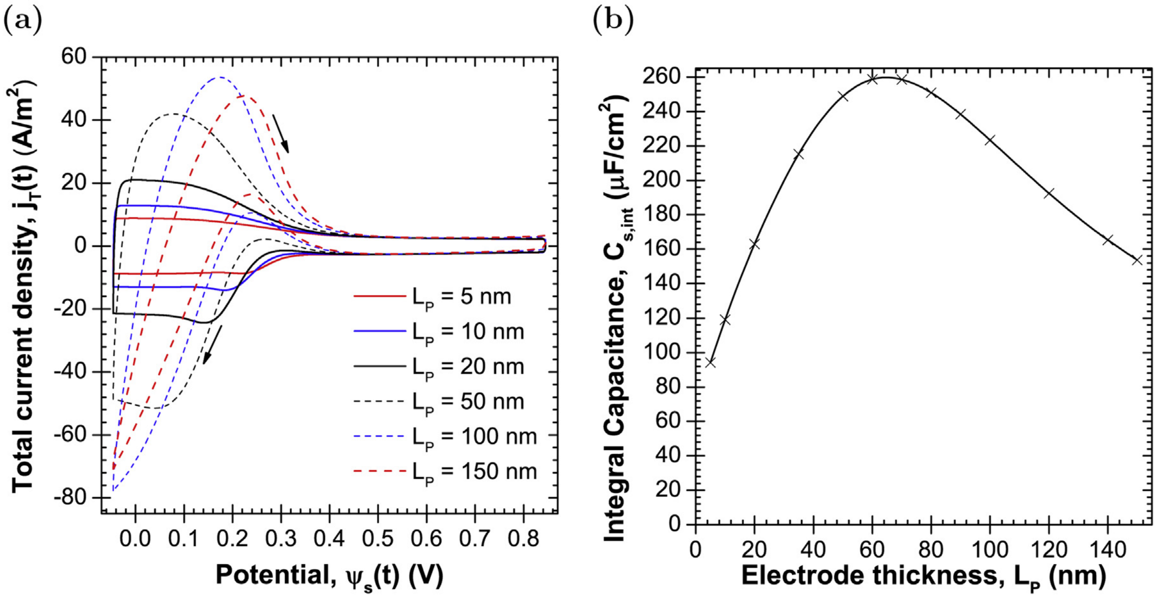

Fig. 6. (a) Numerically predicted total current density j_T (A/m^2) as a function of imposed potential $\psi_s(t)$ at $v = 1$ V/s for different pseudocapacitive electrode thicknesses ranging from 5 to 150 nm. (b) Integral capacitance $C_{s,int}$ as a function of electrode thickness. All other parameters are identical to the baseline case.

electrode was relatively thick. This corroborated the findings of our recent scaling analysis for two-electrode devices captured by the dimensionless number Π_f [11].

4. Conclusion

This paper presented unequivocal physical interpretation of experimentally measured CV curves reported for Nb_2O_5 pseudocapacitive electrodes. First, the numerical simulations of cyclic voltammetry reproduced the behaviors observed experimentally [5,6,26]. Two regimes were identified in the CV curves (i) a faradaic regime dominated by redox reactions and (ii) a capacitive regime dominated by EDL formation as discussed extensively in our previous studies [10,11]. The transition between the regimes was shown to be caused by Li^+ starvation in the electrolyte due to the electrostatic repulsion associated with the ClO_4^- EDL formation. This transition coincided with the dip in the *b*-value commonly observed experimentally. This was further illustrated by comparing CV curves in terms of specific current (A/g) for pseudocapacitive (Nb_2O_5) and EDLC (carbon) electrodes. In addition, the larger current obtained with crystalline vs. amorphous Nb_2O_5 electrodes was attributed to the combination of faster Li intercalation and smaller electrical resistance. Finally, the design trade-off between a thick electrode for achieving large energy storage or capacitance and a thin electrode for minimizing potential drop across the electrode and resistive losses was illustrated leading to an optimal electrode thickness of about 65 nm. Further research should focus on quantitative comparison with experimental data by simulating realistic three-dimensional porous electrode architectures.

Acknowledgements

This material is based upon work supported as part of the Molecularly Engineered Energy Materials, an Energy Frontier Research Center funded by the U.S. Department of Energy, Office of Science, Office of Basic Energy Sciences under Award Number DE-SC0001342. Partial support for the research was also provided by the Office of Naval Research.

Appendix A. Governing Equations and Boundary Conditions

A.1. Governing equations

The local electric potential $\psi(x, t)$ in the pseudocapacitive $(-L_P - L \leq x \leq -L)$ electrode is governed by the one-dimensional Poisson equation expressed as [9,22]

$$\frac{\partial}{\partial x}\left(\sigma_P \frac{\partial \psi}{\partial x}\right) = 0 \tag{2}$$

where σ_P is the electrical conductivity of the electrode.

The local molar concentration of intercalated Li atoms in the pseudocapacitive electrode, denoted by $c_{1,P}(x, t)$, is governed by the mass diffusion equation given by [22,31]

$$\frac{\partial c_{1,P}}{\partial t} = \frac{\partial}{\partial x}\left(D_{1,P} \frac{\partial c_{1,P}}{\partial x}\right) \tag{3}$$

where $D_{1,P}$ is the diffusion coefficient of intercalated lithium atoms in the electrode.

Moreover, the potential and ion concentrations in the diffuse layer of the electrolyte solution $(-L + H \leq x \leq 0)$ are governed by the generalized modified Poisson-Nernst-Planck (GMPNP) model derived by Wang *et al.* [9]. For a binary and symmetric electrolyte the GMPNP in the diffuse layer is expressed as [9]

$$\begin{cases} \dfrac{\partial}{\partial x}\left(\epsilon_0 \epsilon_r \dfrac{\partial \psi}{\partial x}\right) = -F \displaystyle\sum_{i=1}^{2} z_i c_i & \text{(4a)} \\[2ex] \dfrac{\partial c_i}{\partial t} = -\dfrac{\partial N_i}{\partial x} \quad \text{for } i = 1,2 & \text{(4b)} \end{cases}$$

where $c_i(x, t)$ is the local molar concentration of ion species i in the electrolyte solution at time t. Here, $i = 1$ refers to Li^+ and $i = 2$ refers to ClO_4^-. Moreover, $F = 96\,485$ C mol^{-1} is the Faraday constant, $\epsilon_0 = 8.854 \times 10^{-12}$ F m^{-1} is the free space permittivity, and ϵ_r is the relative permittivity of the electrolyte solution. The local mass flux of ion species i, denoted by $N_i(x, t)$ in mol m^{-2}s^{-1}, is defined for a binary and symmetric electrolyte as [9]

$$N_i(x,t) = -D_i \frac{\partial c_i}{\partial x} - \frac{D_i F z_i c_i}{R_u T}\frac{\partial \psi}{\partial x} - \frac{D_i c_i}{1 - \sum_{j=1}^{2} c_j/c_{j,\max}} \frac{\partial}{\partial x}\left(\sum_{j=1}^{2} c_j/c_{j,\max}\right) \tag{5}$$

where D_i and a_i are the diffusion coefficient and the effective ion diameter of ion species i in the electrolyte solution, respectively. The temperature is denoted by T (in K) while $N_A = 6.022 \times 10^{23}$ mol^{-1} and $R_u = 8.314$ J K^{-1}mol^{-1} are the Avogadro constant and the universal gas constant, respectively. The maximum concentration $c_{j,\max} = 1/(N_A a_j^3)$ corresponds to simple cubic ion packing at the electrode surface. The first and second terms of Equation (5) represent the ion flux due to diffusion and electromigration, respectively, while the last term represents a correction accounting for finite ion size [9]. Finally, the presence of a Stern layer near the electrode was accounted for via boundary conditions [32,9] and no governing equations for $\psi(x, t)$ and $c_i(x, t)$ needed to be formulated or solved within the Stern layer.

A.2. Boundary and initial conditions

The one-dimensional governing Equations (2) to (5) are second-order partial differential equations in space and first-order in time. Each equation requires two boundary conditions and one initial condition in each region it is solved.

First, the initial electric potential was assumed to be uniform across the device and given by

$$\psi(x, 0) = 0\,\text{V}. \tag{6}$$

Initially, the Li^+ and ClO_4^- ion concentrations in the electrolyte $(-L + H \leq x \leq 0)$ were taken as uniform and equal to their bulk concentrations satisfying electroneutrality according to

$$c_1(x, 0) = c_{1,\infty} \quad \text{and} \quad c_2(x, 0) = -z_1 c_{1,\infty}/z_2. \tag{7}$$

Similarly, the initial Li concentration in the pseudocapacitive electrode $(-L - L_P \leq x \leq -L)$ was uniform and equal to $c_{1,P,0}$, i.e.,

$$c_{1,P}(x, 0) = c_{1,P,0}. \tag{8}$$

The potential at the current collector/pseudocapacitive electrode interface was imposed as $\psi(-L - L_P,\ t) = \psi_s(t)$. During cyclic voltammetry measurements, $\psi_s(t)$ varied linearly with time according to [9]

$$\Psi_s(t) = \begin{cases} \Psi_{\max} - v[t - (\mathrm{n_c} - 1)\tau_{\mathrm{CV}}] & \text{for } (\mathrm{n_c} - 1)\tau_{\mathrm{CV}} \leq \mathrm{t} < (\mathrm{n_c} - 1/2)\tau_{\mathrm{CV}} \\ \Psi_{\min} + v[t - (\mathrm{n_c} - 1/2)\tau_{\mathrm{CV}}] & \text{for } (\mathrm{n_c} - 1/2)\tau_{\mathrm{CV}} \leq \mathrm{t} < \mathrm{n_c}\tau_{\mathrm{CV}} \end{cases} \tag{9}$$

where n_c is the cycle number and τ_{CV} is the cycle period while ψ_{max} and ψ_{min} are the maximum and minimum values of the cell potential $\psi_s(t)$, respectively. In addition, the potential in the bulk of the electrolyte $(x = 0)$ was set as $\psi(x = 0, t) = 0$ V. The ion concentrations $c_1(x, t)$ and $c_2(x, t)$ were imposed to be constant at $x = 0$ and equal to their bulk concentrations, i.e., $c_1(0, t) = c_2(0, t) = c_{1,\infty}$.

The electric potential varied linearly across the Stern layer so that the electric field at the pseudocapacitive electrode satisfied [32,9]

$$-\frac{\partial \psi}{\partial x}(-L + H, t) = \frac{1}{H}\left[\psi(-L, t) - \psi(-L + H, t)\right] \tag{10a}$$

This boundary condition accounted for the presence of the Stern layers at the electrode surface without explicitly simulating them in the computational domain [32].

The current density at the pseudocapacitive electrode/electrolyte interface, located at $x = -L$ was equal to the sum of the capacitive $j_C(x, t)$ and faradaic $j_F(t)$ current densities (in A/m^2) at the Stern/diffuse interfaces, located at $x = -L + H$, so that [9,21]

$$-\sigma_P \frac{\partial \psi}{\partial x}(-L, t) = j_C(-L + H, t) + j_F(-L + H, t) \tag{11}$$

where, $j_C(x, t)$ is the displacement current density due to the electric double layer formation at the pseudocapacitive electrode surface and defined as [33]

$$j_C(-L + H, t) = -\epsilon_0 \epsilon_r \frac{\partial^2 \psi}{\partial x \partial t}(-L + H, t). \tag{12}$$

In addition, the faradaic current density $j_F(t)$ is typically described by the generalized Frumkin-Butler-Volmer model evaluated at the pseudocapacitive electrode/electrolyte interface and expressed as [13]

$$j_F(t) = j_{F,0}(t)\{\exp[\frac{(1-\alpha)z_1F\eta}{R_uT}] - \exp[\frac{-\alpha z_1F\eta}{R_uT}]\} \tag{13}$$

where $\eta = \Delta\psi_H - \Delta\psi_{eq}$ is the overpotential and $\Delta\psi_H = \psi(-L, t) - \psi(-L+H, t)$ is the electrical potential drop across the Stern layer near the pseudocapacitive electrode [13]. For electrodes made of transition metal oxides, the equilibrium potential difference $\Delta\psi_{eq}$ is typically fitted experimentally as a function of the state-of-charge $c_{1,P}/c_{1,P,max}$ where $c_{1,P,max}$ is the maximum concentration of intercalated lithium atoms in the pseudocapacitive electrode [34–36]. It can be obtained by fitting experimental data for the open-circuit potential [21,22], as illustrated by Eq. (1). The so-called exchange current density $j_{F,0}(t)$ can be written as [21,22]

$$j_{F,0}(t) = Fz_1k_0[c_1(-L+H,t)]^{1-\alpha}[c_{1,P,\max} - c_{1,P}(-L,t)]^{\alpha}[c_{1,P}(-L,t)]^{\alpha} \tag{14}$$

where k_0 is the reaction rate constant expressed in $\mathrm{m}^{1+3\alpha}\mathrm{mol}^{-\alpha}\mathrm{s}^{-1}$. Here, the transfer coefficient α was assumed to be 0.5, corresponding to identical energy barriers for forward and backward redox reactions [13]. In this case, the faradaic current $j_F(t)$ has the same sign as the overpotential $\eta(t)$.

Moreover, the current collector was impermeable to the lithium atoms intercalated in the pseudocapacitive electrode so that the mass flux of Li vanished at the pseudocapacitive electrode/current collector interface (at $x = -L-L_P$), i.e.,

$$-D_{1,P}\frac{\partial c_{1,P}}{\partial x}(-L-L_P, t) = 0\,\mathrm{mol\,m^{-2}\,s^{-1}}. \tag{15}$$

The mass flux of Li exiting through the pseudocapacitive electrode/electrolyte interface ($x = L$) was related to the faradaic current density $j_F(t)$ based on stoichiometry as

$$-D_{1,P}\frac{\partial c_{1,P}}{\partial x}(-L, t) = \frac{j_F(t)}{z_1F}. \tag{16}$$

The mass flux of Li^+ ions ($i = 1$) across the Stern/diffuse layer interface near the pseudocapacitive electrode was related to $j_F(t)$ in the same way such that

$$N_1(-L+H, t) = \frac{j_F(t)}{z_1F}. \tag{17}$$

Finally, the pseudocapacitive electrode was impermeable to ClO_4^- ions ($i = 2$) so that

$$N_2(-L+H, t) = 0\,\mathrm{mol\,m^{-2}\,s^{-1}}. \tag{18}$$

References

[1] P. Simon, Y. Gogotsi, Materials for Electrochemical Capacitors, Nat. Mater. 7 (2008) 845–854.

[2] Y. Zhang, H. Feng, X. Wu, L. Wang, A. Zhang, T. Xia, H. Dong, X. Li, L. Zhang, Progress of Electrochemical Capacitor Electrode Materials: a Review, Int. J. Hydrogen Energy 34 (2009) 4889–4899.

[3] Z.-S. Wu, G. Zhou, L.-C. Yin, W. Ren, F. Li, H.-M. Cheng, Graphene/Metal Oxide Composite Electrode Materials for Energy Storage, Nano Energy 1 (2012) 107–131.

[4] G. Wang, L. Zhang, J. Zhang, A Review of Electrode Materials for Electrochemical Supercapacitors, Chem. Soc. Rev. 41 (2012) 797–828.

[5] V. Augustyn, J. Come, M.A. Lowe, J.W. Kim, P.-L. Taberna, S.H. Tolbert, H.D. Abruña, P. Simon, B. Dunn, High-Rate Electrochemical Energy Storage through Li^+ Intercalation Pseudocapacitance, Nat. Mater. 12 (2013) 518–522.

[6] J.W. Kim, V. Augustyn, B. Dunn, The Effect of Crystallinity on the Rapid Pseudocapacitive Response of Nb_2O_5, Adv. Energy Mater. 2 (2012) 141–148.

[7] J. Come, V. Augustyn, J.W. Kim, P. Rozier, P.-L. Taberna, P. Gogotsi, J.W. Long, B. Dunn, P. Simon, Electrochemical Kinetics of Nanostructured Nb_2O_5 Electrodes, J. Electrochem. Soc. 161 (2014) A718–A725.

[8] L. Pilon, H. Wang, A. d'Entremont, Recent Advances in Continuum Modeling of Interfacial and Transport Phenomena in Electric Double Layer Capacitors, J. Electrochem. Soc. 162 (2015) A5158–A5178.

[9] H. Wang, A. Thiele, L. Pilon, Simulations of Cyclic Voltammetry For Electric Double Layers In Asymmetric Electrolytes: A Generalized Modified Poisson-Nernst-Planck Model, J. Phys. Chem. C 117 (2013) 18286–18297.

[10] H.-L. Girard, H. Wang, A. d'Entremont, L. Pilon, Physical Interpretation of Cyclic Voltammetry for Hybrid Pseudocapacitors, J. Phys. Chem. C 119 (2015) 11349–11361.

[11] H.-L. Girard, H. Wang, A.L. d'Entremont, L. Pilon, Enhancing Faradaic Charge Storage Contribution in Hybrid Pseudocapacitors, Electrochim. Acta 182 (2015) 639–651.

[12] A. d'Entremont, L. Pilon, Electrochemical Transport Phenomena in Hybrid Pseudocapacitors Under Galvanostatic Cycling, J. Electrochem. Soc. (2015) (accepted).

[13] A.J. Bard, L.R. Faulkner, Electrochemical Methods: Fundamentals and Applications, John Wiley & Sons, New York, NY, 2001.

[14] G.J. Janz, R.P.T. Tomkins, Nonaqueous Electrolytes Handbook, Vol. I, Academic Press, New York, NY, 1972.

[15] K. Nishikaw, Y. Fukunaka, T. Sakka, Y.H. Ogata, J.R. Selman, Measurement of $LiClO_4$ Diffusion Coefficient in Propylene Carbonate by Moire Pattern, J. Electrochem. Soc. 153 (2006) 830–834.

[16] M.C. López, G.F. Ortiz, P. Lavela, R. Alcántara, J.L. Tirado, Improved Energy Storage Solution Based on Hybrid Oxide Materials, ACS Sustainable Chem. Eng. 1 (2013) 46–56.

[17] Y.-P. Lin, N.-L. Wu, Characterization of $MnFe_2O_4/LiMn_2O_4$ Aqueous Asymmetric Supercapacitor, J. Power Sources 196 (2011) 851–854.

[18] E. Lim, H. Kim, C. Jo, J. Chun, K. Ku, S. Kim, H.I. Lee, I.-S. Nam, S. Yoon, K. Kang, et al., Advanced Hybrid Supercapacitor Based on a Mesoporous Niobium Pentoxide/Carbon as High-Performance Anode, ACS nano 8 (2014) 8968–8978.

[19] D. Bélanger, T. Brousse, J.W. Long, Manganese Oxides: Battery Materials Make the Leap to Electrochemical Capacitors, Electrochem. Soc. Interface 17 (2008) 49–52.

[20] A.M. Colclasure, R.J. Kee, Thermodynamically Consistent Modeling of Elementary Electrochemistry in Lithium-ion Batteries, Electrochim. Acta 55 (2010) 8960–8973.

[21] S.R. Subramanian, V. Boovaragavan, V. Ramadesigan, M. Arabandi, Mathematical Model Reformulation for Lithium-Ion Battery Simulations: Galvanostatic Boundary Conditions, J. Electrochem. Soc. 156 (2009) 260–271.

[22] G.M. Goldin, A.M. Colclasure, A.H. Wiedemann, R.J. Kee, Three-Dimensional Particle-Resolved Models of Li-ion Batteries to Assist the Evaluation of Empirical Parameters in One-Dimensional Models, Electrochim. Acta 64 (2012) 118–129.

[23] M. Toupin, T. Brousse, D. Bélanger, Charge Storage Mechanism of MnO_2 Electrode Used in Aqueous Electrochemical Capacitor, Chem. Mater. 16 (2004) 3184–3190.

[24] J. Zhu, S. Tang, H. Xie, Y. Dai, X. Meng, Hierarchically Porous MnO_2 Microspheres Doped with Homogeneously Distributed Fe_3O_4 Nanoparticles for Supercapacitors, ACS Appl. Mater. Interfaces 6 (2014) 17637–17646.

[25] P. Guillemet, T. Brousse, O. Crosnier, Y. Dandeville, L. Athouel, Y. Scudeller, Modeling Pseudo Capacitance of Manganese Dioxide, Electrochim. Acta 67 (2012) 41–49.

[26] X. Wang, G. Li, Z. Chen, V. Augustyn, X. Ma, G. Wang, B. Dunn, Y. Lu, High-Performance Supercapacitors Based on Nanocomposites of Nb_2O_5 Nanocrystals and Carbon Nanotubes, Adv. Energy Mater. 1 (2011) 1089–1093.

[27] J. Wang, J. Polleux, J. Lim, B. Dunn, Pseudocapacitive Contributions to Electrochemical Energy Storage in TiO_2 (Anatase) Nanoparticles, J. Phys. Chem. C 111 (2007) 14925–14931.

[28] Y.-M. Lin, P.R. Abel, D.W. Flaherty, J. Wu, K.J. Stevenson, A. Heller, C.B. Mullins, Morphology Dependence of the Lithium Storage Capability and Rate Performance of Amorphous TiO_2 Electrodes, J. Phys. Chem. C 115 (2011) 2585–2591.

[29] L. Shao, J.-W. Jeon, J.L. Lutkenhaus, Porous Polyaniline Nanofiber/Vanadium Pentoxide Layer-by-Layer Electrodes for Energy Storage, J. Mater. Chem. A 1 (2013) 7648–7656.

[30] C.-P. Liu, F. Zhou, V. Ozolins, First Principles Study for Lithium Intercalation and Diffusion Behavior in Orthorhombic Nb_2O_5 Electrochemical Supercapacitor, APS Meeting Abstracts (2012), p 26003.

[31] C. Wang, A.M. Sastry, Mesoscale Modeling of a Li-Ion Polymer Cell, J. Electrochem. Soc. 154 (2007) 1035–1047.

[32] H. Wang, L. Pilon, Mesoscale Modeling of Electric Double Layer Capacitors with Three-Dimensional Ordered Structures, J. Power Sources 221 (2013) 252–260.

[33] H. Cohen, J.W. Cooley, The Numerical Solution of the Time-Dependent Nernst-Planck Equations, Biophys. J. 5 (1965) 145–162.
[34] T. Jow, J. Zheng, Electrochemical Capacitors Using Hydrous Ruthenium Oxide and Hydrogen Inserted Ruthenium Oxide, J. Electrochem. Soc. 145 (1998) 49–52.
[35] G. Sikha, R.E. White, B.N. Popov, A Mathematical Model for a Lithium-ion Battery/Electrochemical Capacitor Hybrid System, J. Electrochem. Soc. 152 (2005) A1682–A1693.
[36] H. Kim, B.N. Popov, A Mathematical Model of Oxide, Carbon Composite Electrode for Supercapacitors, J. Electrochem. Soc. 150 (2003) 1153–1160.